Article

Layered-to-Rock-Salt Transformation in Desodiated Na$_x$CrO$_2$ (x 0.4)

Shou-Hang Bo,[†,‡,⊥] Xin Li,[§,⊥] Alexandra J. Toumar,[†] and Gerbrand Ceder*[,†,‡,∥]

[†]Department of Materials Science and Engineering, Massachusetts Institute of Technology, Cambridge, Massachusetts 02139, United States

[‡]Materials Science Division, Lawrence Berkeley National Laboratory, Berkeley, California 94720, United States

[§]John A. Paulson School of Engineering and Applied Sciences, Harvard University, Cambridge, Massachusetts 02138, United States

[∥]Department of Materials Science and Engineering, University of California, Berkeley, California 94720, United States

S *Supporting Information*

ABSTRACT: O3 layered sodium transition metal oxides (i.e., NaMO$_2$, M = Ti, V, Cr, Mn, Fe, Co, Ni) are a promising class of cathode materials for Na-ion battery applications. These materials, however, all suffer from severe capacity decay when the extraction of Na exceeds certain capacity limits. Understanding the causes of this capacity decay is critical to unlocking the potential of these materials for battery applications. In this work, we investigate the structural origins of capacity decay for one of the compounds in this class, NaCrO$_2$. The (de)sodiation processes of NaCrO$_2$ were studied both *in situ* and *ex situ*

through X-ray and electron diffraction measurements. We demonstrate that Na$_x$CrO$_2$ ($0 < x < 1$) remains in the layered structural framework without Cr migration up to a composition of Na$_{0.4}$CrO$_2$. Further removal of Na beyond this composition triggers a layered-to-rock-salt transformation, which converts P′3-Na$_{0.4}$CrO$_2$ into the rock-salt CrO$_2$ phase. This structural transformation proceeds via the formation of an intermediate O3 Na$_\delta$CrO$_2$ phase that contains Cr in both Na and Cr slabs and shares very similar lattice dimensions with those of rock-salt CrO$_2$. It is intriguing to note that intercalation of alkaline ions (i.e., Na$^+$ and Li$^+$) into the rock-salt CrO$_2$ and O3 Na$_\delta$CrO$_2$ structures is actually possible, albeit in a limited amount (∼0.2 per formula unit). When these results were analyzed under the context of electrochemistry data, it was apparent that preventing the layered-to-rock-salt transformation is crucial to improve the cyclability of NaCrO$_2$. Possible strategies for mitigating this detrimental phase transition are proposed.
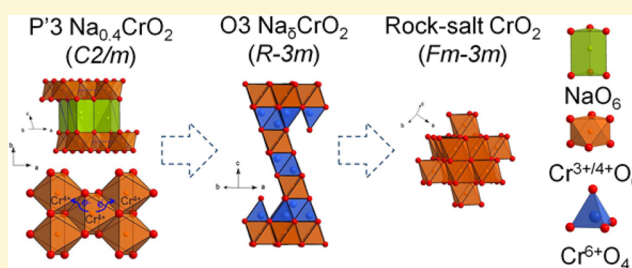
INTRODUCTION

Although Li-ion batteries are still the dominant contender in portable electronics, the inhomogeneous global distribution of lithium could pose a significant challenge for the widespread use of Li-ion batteries in large-scale applications, such as electric vehicles and grid-scale energy storage. Seeking abundant and affordable alternatives is therefore extremely important for a sustainable energy future. Na-ion battery technology is one of the most promising solutions to power large-scale devices because of the wide availability of sodium resources and the potentially richer electrode chemistry compared with that of its lithium counterpart.[1−5] Since the revival of research interest in Na-ion batteries in the early 2000s, we have witnessed a rapid development of this field, as manifested in the discovery of a myriad of new electrode materials.[6−13]

Among the cathode materials studied to date, NaMO$_2$ (M = Ti, V, Cr, Mn, Fe, Co, Ni) compounds represent a particularly promising class of materials because of their high volumetric and gravimetric energy densities.[14−21] All seven NaMO$_2$ materials possess an ordered rock-salt structure, i.e., an O3 or O′3 layered structure where O indicates octahedrally coordinated Na, 3 indicates a repeated stacking period of three layers, and the prime sign indicates the presence of

monoclinic distortion.[22] The significant charge and size differences between Na and the 3d transition metal create alternating Na and transition metal slabs along the layer stacking direction. During charge or desodiation, these phases undergo successive phase transitions, and the desodiated phases are commonly observed in either the O3 (or O′3) or P3 (or P′3) structure, accompanied by layer spacing variation, complex Na-vacancy ordering evolution, and possible monoclinic distortion. The P3 (or P′3) structure shares the same repeating period as O3 (or O′3) but differs in the coordination environment of Na (i.e., prismatically coordinated Na).

All of the seven transition metal oxides (i.e., NaMO$_2$) were demonstrated to be able to reversibly cycle against Na within certain capacity limits (approximately 0.5 Na per formula unit in most cases). When the Na extraction exceeds this limit, however, these transition metal oxides invariably exhibit severe capacity decay. NaTiO$_2$ is likely the best material among the single transition metal systems in terms of capacity retention. When cycled between the compositions of NaTiO$_2$ and

$Na_{0.4}TiO_2$, 98% of the initial capacity can still be maintained after 60 cycles. However, if >0.7 Na is removed during the initial charge, then the subsequent discharge capacity drastically decreases to ~0.4 Na insertion.[19] A very similar scenario also occurs in $NaVO_2$,[18] $NaCoO_2$,[23] and $NaNiO_2$.[14] Highly reversible Na intercalation can be achieved when limiting the charge process to a composition near $Na_{0.5}MeO_2$ (Me = V, Co, Ni), beyond which the capacity decay starts to be pronounced. $NaCrO_2$[17] and $NaFeO_2$,[21,24] however, become almost inactive if more than 0.5 or 0.35 Na is removed during the first charge, respectively. $NaMnO_2$ exhibits different electrochemistry characteristics as it can deliver a reversible capacity corresponding to approximately 0.8 Na in the first cycle. Still, this capacity rapidly decays to only 0.6 Na within 10 cycles.[16] Therefore, it is critical to understand the fundamental limiting factors for capacity fade in this family of layered sodium compounds.

The capacity fade of these O3 $NaMO_2$ materials has been related to irreversible structural transitions near the end of full Na extraction, including transition metal migration[18−20,24,25] and water/CO_2 intercalation into the Na layer.[26−28] In both cases, the Na diffusion channels will presumably be blocked, resulting in a reduced degree of Na insertion based on kinetic considerations. Transition metal migration may cause a layer spacing shrinkage as the migration of a high valence transition metal ion (usually ≥3+) into the Na layer will induce a strong electrostatic attraction between the transition metal and O layers above and below. This type of phenomenon has been observed in the $NaTiO_2$ system.[19,20] However, layer spacing shrinkage is not necessarily correlated with the transition metal migration, as evidenced in our prior theory calculation in the lithium analogue[29] and our recent experimental investigation of a quaternary O3 compound.[10] Water/CO_2 intercalation was often observed when the as-prepared materials experienced ambient atmosphere exposure. It is unclear, however, if the same phenomenon would also occur during battery cycling, where the water and CO_2 contents are minimal in the closed system.

We used $NaCrO_2$ as a representative system to investigate the instabilities at the top of the charge. The desodiation process in $NaCrO_2$ was first investigated by Delmas et al. and Miyazaki et al. in the 1980s through electrochemical and chemical means, respectively.[30,31] In the electrochemical desodiation work performed by Delmas and co-workers, a reversible Na intercalation process was observed between the compositions of $NaCrO_2$ and $Na_{0.85}CrO_2$.[30] A major advance in the electrochemical performance of $NaCrO_2$ came about 30 years later when Komaba and co-workers demonstrated a reversible intercalation of 0.5 Na per formula unit (~125 mAh/g).[17] In 2012, Xia and co-workers demonstrated that $Na_{0.5}CrO_2$ is an intrinsically safe compound, which exhibits even better thermal stability than those of $Li_{0.5}CoO_2$ and fully delithiated $LiFePO_4$.[32] This finding proves that $NaCrO_2$ possesses improved safety features compared with those of commercially available cathodes, such as $LiCoO_2$ and $LiFePO_4$. Very recent work on carbon-coated $NaCrO_2$ demonstrated the unprecedented rate capability of this compound, where a capacity of 100 mAh/g can still be maintained at an extremely high rate of 150 C (i.e., 24 s to fully charge the battery), making $NaCrO_2$ one of the highest-power-density electrode materials.[33]

The structural transitions of $NaCrO_2$ during desodiation were investigated through *ex situ* and *in situ* X-ray diffraction (XRD) by the groups of Komaba and Yang, respectively.[25,34] Both of these works suggest that $NaCrO_2$ evolves from an initial O3 structure to an O′3 and later a P′3 structure during the course of electrochemical desodiation. Of note is that these two studies limited the desodiation process to $Na_{0.5}CrO_2$, where the capacity fade remains minimal. A very recent study by Komaba and co-workers attempted to characterize the structures in Na_xCrO_2 that was charged beyond the composition of $Na_{0.5}CrO_2$ through a combination of XRD, X-ray absorption spectroscopy (XAS), and density functional theory (DFT) calculations.[35] On the basis of the differences of X-ray absorption (XAS) responses from octahedrally and tetrahedrally coordinated Cr, they argued that part of the Cr ions migrates from the original octahedral sites to tetrahedral sites after charging to 4.5 V (this voltage and all subsequent voltages are relative to Na^+/Na, unless otherwise specified). By comparing the experimental diffraction patterns with simulated ones, they also proposed that Cr migration produced an O′3 layered Na_xCrO_2 ($x \sim 0.06$) phase, in which one layer with both tetrahedrally and octahedrally coordinated Cr and another layer with only octahedrally coordinated Cr were stacked on top of each other. However, as will be discussed in this article, our combined synchrotron X-ray and electron diffraction study suggests that the O′3 phase identified in the previous work conducted by Komaba's group is, in fact, a two-phase mixture, i.e., a layered phase (O3 $Na_\delta CrO_2$) and a rock-salt CrO_2 phase.

In our study, the (de)sodiation processes of $NaCrO_2$ were first characterized by *in situ* XRD. We used a slow cycling rate (C/50) so that the measurement remained close to thermodynamic equilibrium. This *in situ* XRD study guided us in pinpointing the compositions that required a more detailed structural study. *Ex situ* synchrotron XRD and electron diffraction were then performed on samples that were charged to selected stages of charge. Synchrotron XRD allowed us to collect bulk structural information on these samples, whereas selected-area electron diffraction (SAED) offered a unique opportunity to probe the structures of selected domains in any given particle. Through these and complementary electrochemistry and *ab initio* computational data, we demonstrate that P′3 $Na_{0.4}CrO_2$ will transform into a rock-salt CrO_2 phase near the end of full Na removal and that this layered-to-rock-salt transformation is responsible for the capacity fade of $NaCrO_2$.

■ METHODS

Synthesis of $NaCrO_2$. $NaCrO_2$ powder samples were prepared by ball milling stoichiometric amounts of Na_2CO_3 (Alfa Aesar, 99.95%) and Cr_2O_3 (Sigma-Aldrich, 99.9%) precursors. The powder mixture was then pressed into a $^1/_2$ in. pellet. The resulting pellet was placed into an alumina boat and transferred into an alumina tube furnace, which was sealed and purged with Ar. The furnace was then heated at 900 °C with a ramping rate of 5 °C/min under a continuous flow of Ar. The reaction was completed after firing at 900 °C for 5 h. The samples were recovered when the furnace was cooled to room temperature and were immediately transferred to the Ar glovebox.

Electrochemical Tests. $NaCrO_2$ electrodes were prepared by mixing the as-prepared $NaCrO_2$ powder, Super P carbon black, and poly(tetrafluoroethylene) (PTFE) in a weight ratio of 80:15:5 with a mortar and pestle in an Ar glovebox. This powder mixture was rolled into a thin film using a stainless steel plate and roller. Circular disks of $^5/_{16}$ in. diameter were then punched with a loading of approximately 3−5 mg. These electrodes were assembled into Swagelok cells with Na metal as the counter electrode and 1 M $NaPF_6$ in a 1:1 (volumetric ratio) ethylene carbonate/diethyl carbonate (EC/DEC) solvent mixture as the electrolyte. Two glass fiber separators were used in all of the cells that were tested. The charge and discharge of the $NaCrO_2$ batteries were performed with an Arbin battery cycler.

X-ray Diffraction Measurements. To verify the purity of the $NaCrO_2$, laboratory XRD measurements were performed using a PANalytical instrument with a Cu Kα source. The $NaCrO_2$ powder was placed onto a standard glass XRD sample holder sealed with a Kapton film to limit air exposure. Diffraction data for the as-prepared $NaCrO_2$ sample is presented in Figure S1 of the Supporting Information. A home-designed airtight cell was used for the *in situ* XRD measurements. The *in situ* cell was cycled at a rate of C/50. Diffraction data were collected every 2 h during cycling using a Bruker D8 diffractometer with a Mo Kα source. For the *ex situ* synchrotron XRD measurements, samples were prepared by charging $NaCrO_2$ electrodes to selected states of charge and then relaxing under potentiostatic mode (a typical relaxation time of ~2 days). These electrodes were recovered and packed into 0.7 mm diameter special glass capillaries in an argon glovebox. The glass capillary was further secured into a 1 mm diameter Kapton tube. The diffraction data were collected at beamline 11BM at the Advanced Photon Source (APS) of Argonne National Laboratory with a constant wavelength of ~0.41 Å. Of note is that all of the diffraction patterns exhibited a complicated background between 4 and 8° 2θ, which is attributed to the Kapton tube. We round and thus inducing significant errors to the extraction of peak intensities. The Rietveld refinements were performed using the TOPAS 4.2 software package (Bruker).

Electron Microscopy. The TEM samples were prepared by sonicating the cathode film dissembled from the Swagelok cell inside the Ar-filled glovebox, which was then placed onto the copper grid. The SAED patterns were obtained on a JEOL 2010F microscope.

***Ab Initio* Computation.** Several potential P3 and O3 Na-vacancy ordered structures were used to determine low-energy layered structures at each composition considered. Compositions were selected based on active-ion concentrations at which ground states were predicted in Li intercalating oxides, such as Li_xNiO_2.[36] Data analytics were carried out with the aid of the pymatgen Python codebase for materials analysis.[37]

Energy calculations were performed using the Vienna *ab initio* simulation package (VASP)[38] within the projector-augmented wave approach,[39] using the Perdew−Burke−Ernzerhof (PBE) generalized-gradient approximation (GGA)[40] functional with the GGA+U extension.[41] All calculations were spin-polarized and used a plane wave energy cutoff of 520 eV. The U value used for Cr (3.5) was that found by Jain et al.[37] in previous work using Wang et al.'s method[42] to determine U from the formation enthalpies of binary oxides.

■ RESULTS

The electrochemical curve during battery cycling provides indirect yet useful insights into the structural transitions during the (de)sodiation processes of $NaCrO_2$, as it often reflects the intrinsic thermodynamics of the desodiated phases (e.g., Na_xCrO_2), especially at a slow rate. As shown in Figure 1, starting with an open-circuit voltage (OCV) of approximately 2.6 V, charging the $NaCrO_2$ battery at a rate of C/50 to 4 V removes nominally 0.96 Na from the parent phase assuming that no side reactions occur, reaching a composition of ~$Na_{0.04}CrO_2$. It is well-established by others[25,35] that a critical point that distinguishes reversible versus irreversible Na extraction from $NaCrO_2$ occurs near an electrochemical potential of ~3.7 V and a composition of approximately $Na_{0.4}CrO_2$ (C/50; Figure 1). When the cathode is charged beyond this composition, significant capacity decay will occur. For instance, after a first charge to 4 V, the discharge capacity drastically drops to ~0.2 Na insertion per formula unit (Figure 1). The discharge curve is clearly different from the charge curve, suggesting that different structural transition pathways are taken during the charge and discharge processes. In addition, the discharge curve appears to be associated with a large polarization, indicating that this Na insertion process is
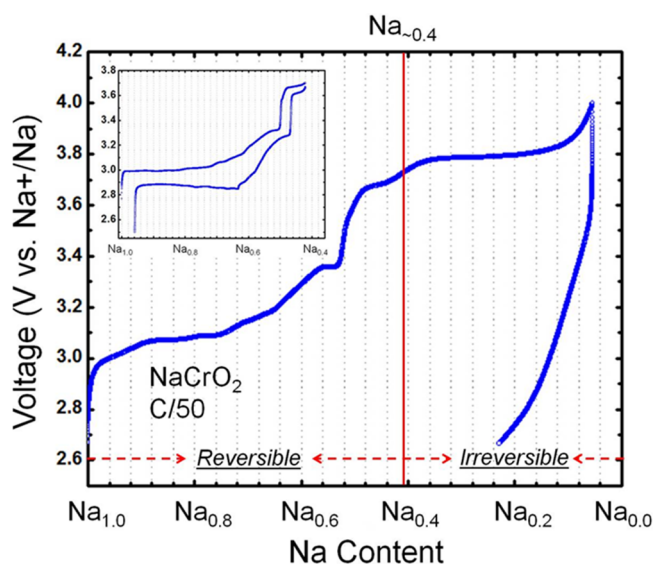

Figure 1. Charge and discharge curves of $NaCrO_2$ at a cycling rate of C/50. "Reversible" and "irreversible" are used to indicate the composition range at which $NaCrO_2$ undergoes (ir)reversible Na intercalation. The inset shows the electrochrochemistry data of the first cycle at the same rate (i.e., C/50) but with a cutoff voltage of 3.7 V.

likely accompanied by large kinetic barriers (discussed in further detail below).

To unravel the causes of capacity fade, it is crucial to understand the desodiation process of $NaCrO_2$ and to determine if the capacity fade is linked to certain structural transitions, in particular, stacking changes, which occur near the composition $Na_{0.4}CrO_2$ (or at approximately 3.7 V). To monitor these phase transitions, we have performed an *in situ* XRD measurement of $NaCrO_2$ during electrochemical cycling. In the following paragraphs, we first review the phases that are often present during the desodiation of an O3 layered oxide and their associated diffraction signatures, followed by an analysis of the *in situ* XRD patterns and a summary of the structural transitions that occur during $NaCrO_2$ desodiation.

Phases with four different structures, i.e., O3 ($R\bar{3}m$, #166), O′3 ($C2/m$, #14), P3 ($R3m$, #160), and P′3 ($C2/m$, #14), are commonly observed in the desodiation process of O3 layered oxides, where the number after the # symbol denotes the space group number following the conventions defined in the International Tables for Crystallography, Volume A. Because the $R\bar{3}m$ and $R3m$ space groups share the same systematic absences and *hkl* reflections, it is impossible to distinguish the O3 and P3 phases by examining only the XRD peak positions. However, the relative XRD intensities of different peaks do vary in the O3 and P3 structures. The most pronounced differences are observed for the 104 and 015 peaks, which provide an effective means to distinguish the O3 and P3 structures. As shown in the simulated XRD patterns of O3 $NaCrO_2$ and a hypothetical P3 $NaCrO_2$ (Figure 2), the 104 peak at a *d*-spacing of ~2.13 Å is much more intense than the 015 peak at ~1.99 Å in the O3 structure; however, the relative intensities of the two peaks are reversed in the P3 structure, which is consistent with previous observations of related materials.[10,34,43−45] The formation of a monoclinic-distorted O′3 (or P′3) phase is signified by a splitting of the peaks corresponding to an O3 (or P3) structure.[44,45] Of note is that structures can become much more complex due to Na-vacancy ordering.[46] Nevertheless, the
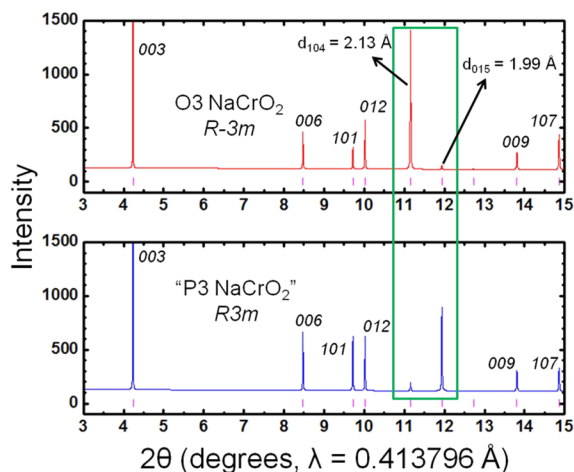
Figure 2. Simulated XRD patterns of O3-NaCrO$_2$ (top) and "P3-NaCrO$_2$" (bottom) with a wavelength of 0.413796 Å, which is typically used at the 11BM beamline at Advanced Photon Source. The green lines are used to highlight the intensity variations of the 104 and 015 peaks in the O3 and P3 structures.

Figure 3. (a) Twenty four *in situ* XRD patterns collected during the first charge of NaCrO$_2$ (C/50). The peak from the Al current collector overlaps with the 104 peak of NaCrO$_2$ at ~19° (2θ) and is marked with an asterisk. (b) Corresponding electrochemistry curve, with the scan numbers marked on top of the curve. The four color shaded regions are used to highlight the four dominant reactions associated with stacking variations that occurred during the desodiation of NaCrO$_2$. The critical compositions at which the switchover between different reaction regimes occurs are also labeled on the top *x* axis.

above analysis regarding the diffraction signatures of O3, O'3, P3, and P'3 should still approximately hold and can be used as a tool in the analysis of XRD patterns.

The *in situ* diffraction measurement was performed at a slow cycling rate of C/50, and diffraction patterns were collected every 2 h, resulting in a total of 24 scans for the first charge (Figure 3a,b). At OCV, five major peaks corresponding to the O3 NaCrO$_2$ pristine phase are presented in the two panels of Figure 3a. These peaks correspond to the 003, 006, 101, 012, and 104 reflections (from lower to higher angles in 2θ) of a $R\bar{3}m$ structure with lattice parameters of $a = b = 2.9694(1)$ Å and $c = 15.984(1)$ Å. The 015 reflection is almost invisible (which is a diffraction signature of the O3 phase, as discussed above). The number of peaks observed near the 003 (~7.5° in 2θ) and 006 (~15° in 2θ) reflections can be taken to indicate the number of phases that are present in the diffraction pattern. For instance, from scans 1 to 7, the left shoulders of the 003 and 006 peaks grow in intensity while the 003 and 006 peaks decrease in intensity, suggesting that a new phase with increased layer spacing along the *c* lattice direction is produced at the expense of the pristine O3 NaCrO$_2$. In addition, the diminishing of the 104 reflection (~19° in 2θ) and the appearance of the 015 reflection (~20.5° in 2θ), as discussed above, signifies a transition from an O3 (or O'3) structure to a P3 (or P'3) structure. A typical example of this transition is observed in scans 7−9, where the intensity of the 015 peak is minimal in scan 7 but grows to be significant in scans 8 and 9.

On the basis of the above analysis and whether monoclinic-distortion-induced peak splitting is present, we can assign the different reaction regimes based on their stacking sequences that are observed during NaCrO$_2$ desodiation (Figure 3b). The initial charge of O3 NaCrO$_2$ produces an O'3 Na$_{0.75}$CrO$_2$ phase (between 2.6 and 3.1 V). Further desodiation of Na$_{0.75}$CrO$_2$ results in the formation of a P'3 Na$_{0.73}$CrO$_2$ phase (~3.1 V). Beyond this composition, an extended P'3 region that spans a capacity of ~0.35 Na is observed, where the structure remains P'3 between Na$_{0.73}$CrO$_2$ and Na$_{0.38}$CrO$_2$ (between 3.1 and 3.75 V). The electrochemistry curve in this compositional range consists of several steps, indicating the existence of Na-vacancy ordering, which has been observed in prior studies.[32,35] When
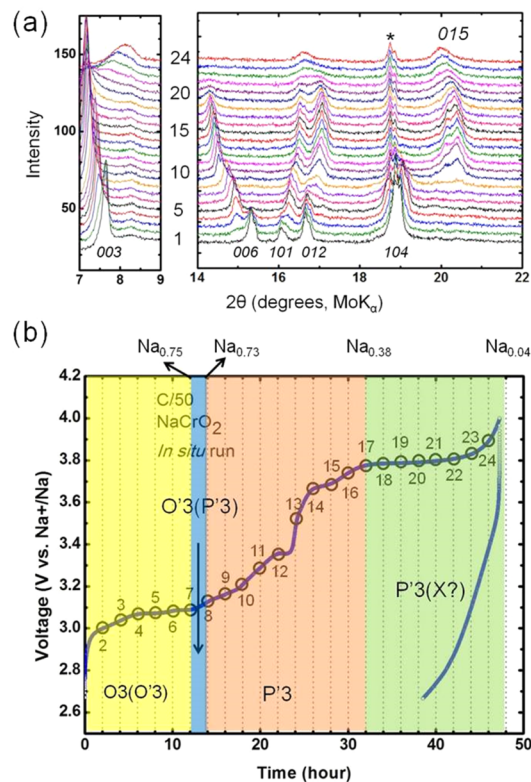
Na is further extracted from the Na$_{0.38}$CrO$_2$ phase, that is, the critical composition where the NaCrO$_2$ electrochemistry becomes irreversible, diffraction peaks corresponding to new phase(s) are clearly present (e.g., the very broad peak at ~8°). The letter X is used in Figure 3b to indicate that one or more unknown phases are produced in the reaction. The conversion between P'3 and X continues until the cutoff voltage of 4 V is reached, where only 0.04 Na remains in the system (estimated from the capacity). Overall, four reaction regimes can be defined during the courses of NaCrO$_2$ desodiation, and these regimes can be divided by three critical compositions, i.e., O'3 Na$_{0.75}$CrO$_2$, P'3 Na$_{0.73}$CrO$_2$, and P'3 Na$_{0.38}$CrO$_2$. Pawley fits for the three phases and their associated lattice parameters are presented in Figure S2 and Table S1, respectively. While we defined the distinct reaction regimes in the desodiation of NaCrO$_2$, the considerably fine structure in the voltage curve indicates a more complex phase diagram, with each area in Figure 3b likely consisting of much smaller single-phase fields separated by second-order or narrow-first-order phase transitions.

The phase transition to X near the composition Na$_{0.4}$CrO$_2$ (or at ~3.7 V) and the significantly decreased discharge capacity once the charge voltage extends beyond 3.8 V (i.e., Figure 3b) suggest that the capacity fade of NaCrO$_2$ is very likely related to this phase transition. To investigate this phase transition in more detail, three samples corresponding to the

beginning, middle, and end of this P′3−X phase transition were prepared and characterized via synchrotron XRD and electron diffraction measurements. The charge curves for the three samples and the corresponding synchrotron XRD patterns are presented in Figure 4.
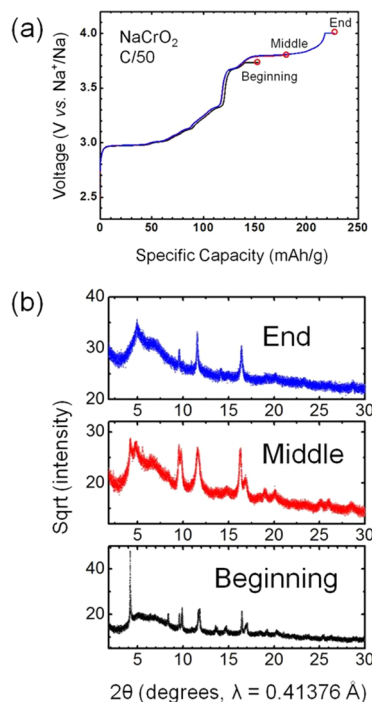

Figure 4. (a) Charge curves for three samples corresponding to the beginning, middle, and end of the P′3−X phase transition and (b) the correponding diffraction patterns.

Starting with the sample that was charged to 3.73 V (or the beginning of the plateau), the diffraction pattern can be indexed with a $C2/m$ space group with lattice parameters of $a = 5.0047(3)$ Å, $b = 2.8839(2)$ Å, $c = 5.8771(6)$ Å, and $\beta = 105.606(4)°$. Because of the reduced occupancy and intrinsic weak scattering power of Na, the occupancy of Na in this desodiated compound cannot be unambiguously determined based on diffraction data only. We have therefore constrained the Na composition to $Na_{0.4}CrO_2$ in the Rietveld refinement, which is the expected Na content based on the extracted charge. Also of note is that the diffraction peaks exhibit strong anisotropic broadening. The phenomenological model of anisotropic peak broadening developed by Stephens was therefore used in the final refinement.[47] As demonstrated in Figure 5, an excellent fit of the experimental data can be obtained using the P′3 structural model. The structural parameters and selected bond lengths are listed in Tables S2−S4. In the refined structure, the Cr−O bond lengths are considerably shortened to 1.928(2) Å (×4) and 1.971(4) Å (×2) relative to those in the pristine $NaCrO_2$ phase (the Cr−O bond length is approximately 2.0 Å), which is consistent with a deintercalation and oxidation process. In addition, the bond valence sum of the Na site (0.95 v.u.) was calculated to be very close to the ideal valence of Na^+ (1.0 v.u.) according to Adam's softBV parameters,[48] further supporting the accuracy of the structural model. All Cr ions occupy octahedral sites in this P′3 structural model, and no Cr ion is found in the Na layer or tetrahedral sites in the Cr layer. This finding is consistent with
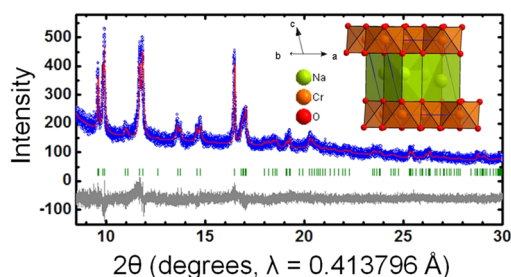

Figure 5. Rietveld refinement of the sample charged to 3.73 V (or the beginning of the 3.8 V plateau), with the observed, calculated, and difference patterns shown in blue, red, and dark gray, respectively. The tick marks corresponding to the $C2/m$ lattice with lattice parameters of $a = 5.0047(3)$ Å, $b = 2.8839(2)$ Å, $c = 5.8771(6)$ Å, and $\beta = 105.606(4)°$ are shown in olive. The refined structure is presented in the inset of the graph.

both our electron diffraction study that will be discussed later (Figure 6e) and prior XAS studies performed by the groups of
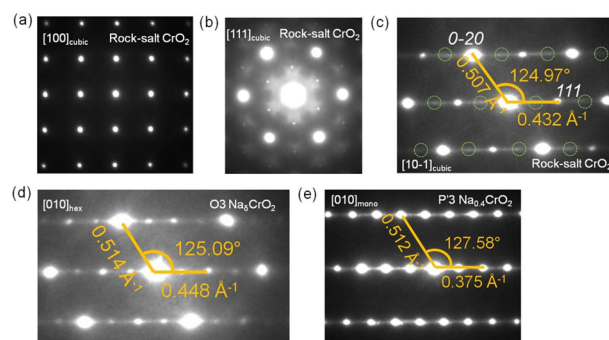

Figure 6. Electron diffraction patterns of the rock-salt CrO_2, O3 $Na_\delta CrO_2$, and P′3 $Na_{0.4}CrO_2$ phases. (a−c) Electron diffraction patterns for the rock-salt CrO_2 viewed along the [100], [111], and [10−1] zone axes, respectively. The subscript "cubic" is used to denote the lattice symmetry. (d, e) Diffraction patterns for the O3 $Na_\delta CrO_2$ and P′3 $Na_{0.4}CrO_2$ phases, which were viewed along the [010] zone axis of the hexagonal and monoclinic lattices, respectively. To better compare the diffraction patterns of rock-salt CrO_2, O3 $Na_\delta CrO_2$, and P′3 $Na_{0.4}CrO_2$, the corresponding diffraction patterns in (c−e) are oriented such that the layer stacking directions all point along the horizontal direction of these images. The green circles in (c) represent the missing reflections, which should be present in the layered phase, such as in (e). Selected distances (in units of Å^{-1}) and angles are labeled in (c−e) to compare with the values of an ideal cubic lattice.

Komaba and Yang, where they also observed that tetrahedrally coordinated Cr ions were not present at similar compositions.[34,35] The fact that Cr does not migrate at this stage is consistent with the reversible Na intercalation between the compositions of $NaCrO_2$ and $Na_{0.4}CrO_2$.

At the end of the 3.8 V plateau, the XRD signature of a layered structure (i.e., the diffraction peak at approximately 5° in 2θ or 4.8 Å in d-spacing) almost completely disappears (Figure 4b). Instead, we observed the formation of a rock-salt phase (Figure 6a−c) through electron diffraction patterns viewed along three different zone axes (i.e., [100], [111], and [10−1]). In an ideal cubic lattice, such as the rock-salt structure, the angle between the (111) and (0−20) points in the reciprocal space should be precisely 125.3°. Consistently, we observed that the angle between the (111) and (0−20) reciprocal-space points of the rock-salt CrO_2 is 125.0° (Figure

6c), which agrees well with the ideal value within the instrumental error bar of approximately 1° on this microscope. Another measure for the cubic lattice is the ratio of d^*_{111} and d^*_{0-20}, which should be $(\sqrt{3}/2)$ or ~0.866. The observed ratio in the rock-salt CrO_2 (Figure 6c) is 0.852, which is substantially closer to the ideal value of 0.866 compared with the ratio observed in the P′3 $Na_{0.4}CrO_2$ phase (i.e., 0.732; Figure 6e), further confirming the cubic symmetry of the rock-salt CrO_2. Noting that nominally only 0.04 Na remains at the end of charge, the transformation to a rock-salt CrO_2 phase is certainly plausible because the driving force for an ordered rock-salt structure to form, i.e., the simultaneous presence of Na^+ and Cr^{3+} as in $NaCrO_2$, is no longer present. We also observed additional scattering spots accompanied by noticeable diffuse scattering intensities in the electron diffraction pattern viewed along the [111] zone axis (Figure 6b), which should otherwise be forbidden in the rock-salt ($Fm\bar{3}m$, #225) symmetry. These data indicate the likely presence of short-range Cr-vacancy ordering. In a rock-salt structure, every cation is surrounded by 6 anions, forming the first coordination sphere, and the second coordination sphere is formed by 12 cations. It is very likely that in the rock-salt CrO_2 structure the nearest 12 octahedral sites surrounding an occupied Cr octahedral site are preferentially empty to minimize the $Cr^{4+}-Cr^{4+}$ electrostatic repulsion, thus giving rise to the additional scattering spots and diffuse scattering observed in Figure 6b. Among the many particles that we surveyed, a few particles exhibit a slightly different electron diffraction pattern, as observed in Figure 6d. This diffraction pattern contains a set of additional diffraction spots that are forbidden in the rock-salt symmetry, as we mentioned earlier in Figure 6c. However, the intensity modulation of this pattern highly resembles rock-salt symmetry, which is very different from a classical layered symmetry (i.e., $R\bar{3}m$ or $R3m$), as shown in Figure 6e. This pattern may be assigned to a mixture of rock-salt CrO_2 and a O3 phase or, more likely, a O3 ($R\bar{3}m$) layered structure with very close lattice parameters and symmetry to those of the rock-salt structure, as evidenced by the distances/angles shown in Figure 6c,d as well as the Rietveld analysis of the synchrotron XRD data (discussed in further detail below). The close similarity between O3 $Na_\delta CrO_2$ and rock-salt CrO_2 indicates that the O3 $Na_\delta CrO_2$ phase may serve as an intermediate phase for the layered (i.e., P′3 $Na_{0.4}CrO_2$) to rock-salt CrO_2 transformation, a conclusion that is also supported by synchrotron XRD data, as will be discussed below.

To better understand the structures of the rock-salt and O3 $Na_\delta CrO_2$ phases, we performed Rietveld analysis of the synchrotron XRD data for samples that were either charged to the end or the middle of the P′3−X phase transition. On the basis of electron diffraction data, the sample that was charged to the end of the 3.8 V plateau should be a two-phase mixture (O3 $Na_\delta CrO_2$ and rock-salt CrO_2). Similarly, the sample that was charged to the middle of the 3.8 V plateau is most likely a three-phase mixture (P′3 $Na_{0.4}CrO_2$, O3 $Na_\delta CrO_2$, and rock-salt CrO_2). The Rietveld refinements were therefore first performed based on a two-phase model for the diffraction data of the sample that was charged to the end of the 3.8 V plateau to extract structural information for the O3 $Na_\delta CrO_2$ and rock-salt CrO_2 phases. The structural parameters (i.e., atomic positions, occupancies, and thermal parameters) for the O3 $Na_\delta CrO_2$, rock-salt CrO_2, and P′3 $Na_{0.4}CrO_2$ phases were then fixed while allowing the scale factors and lattice parameters to vary in the analysis of the diffraction data for the sample that

was charged to the middle of the 3.8 V plateau. In a typical rock-salt structure ($Fm\bar{3}m$, #225), the anions (e.g., O^{2-}) occupy the 4b Wyckoff site (0.5, 0.5, 0.5), producing one octahedral crystallographic site [4a at (0,0,0)] and one crystallographic tetrahedral site [8c at (0.25, 0.25, 0.25)] per unit cell which host the cations. The structure of an O3 compound is slightly more complicated. The O atoms occupy the 6c Wyckoff site $(0,0,z)$, and there are two distinct octahedral [3a (0,0,0) and 3b (0,0,0.5) sites] and tetrahedral sites [two 6c $(0,0,z)$ sites] that can potentially accommodate cations (e.g., Cr^{n+}). In the refinement, we tested the occupancy of Cr on all of the possible octahedral and tetrahedral sites in the rock-salt and O3 structures but constrained the composition of these two phases to be CrO_2 (note the very small concentration of Na has negligible impact on the diffraction data, and the occupancy of Na was therefore excluded from the refinement). We also assumed that tetrahedrally coordinated Cr has a formal charge of 6+ because in most alkaline Cr oxides Cr situated in a tetrahedral site is 6+. This assumption sets the maximal concentration of Cr on tetrahedral sites to be $1/3$, as a higher concentration will cause the remaining Cr to be lower than 3+.

The refinement results provide important information regarding the possibility of Cr migration and the relationship between the O3 $Na_\delta CrO_2$ and rock-salt CrO_2. As demonstrated in Figure 7, use of the two-phase model (rock-salt CrO_2 + O3
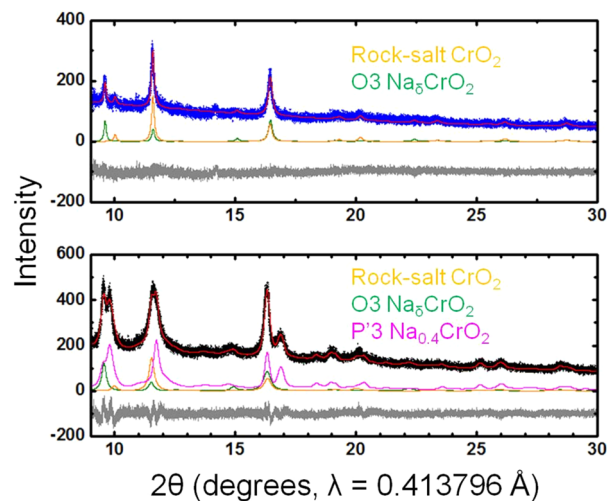

Figure 7. Rietveld refinements for the samples that were charged to the middle and end of the 3.8 V plateau. The experimental data are shown in black for the sample that was charged to the middle of the plateau and in blue for the sample that was charged to the end of the plateau. The calculated and difference patterns are shown in red and dark gray, respectively. Individual contributions for P′3 $NaCr_{0.4}CrO_2$ (magenta), O3 $Na_\delta CrO_2$ (green), and rock-salt CrO_2 (dark yellow) are also displayed.

$Na_\delta CrO_2$) yields an excellent fit for the diffraction data of the sample that was charged to 4 V. The structural parameters of rock-salt CrO_2 and O3 $Na_\delta CrO_2$ are tabulated in Tables S5 and S6, respectively. The close similarity of the rock-salt CrO_2 and O3 $Na_\delta CrO_2$ phases is reflected in their lattice parameters. The cell dimensions of the rock-salt CrO_2 phase are $a = b = c = 4.0778(9)$ Å, and those of the O3 $Na_\delta CrO_2$ ($R\bar{3}m$, #166) are $a = b = 2.8797(6)$ Å, $c = 14.169(6)$ Å. $R\bar{3}m$ is a maximal nonisomorphic subgroup of $Fm\bar{3}m$, and one can transform the unit cell of $Fm3m$ to the $R\bar{3}m$ lattice using the following 3 × 3 matrix:[49]
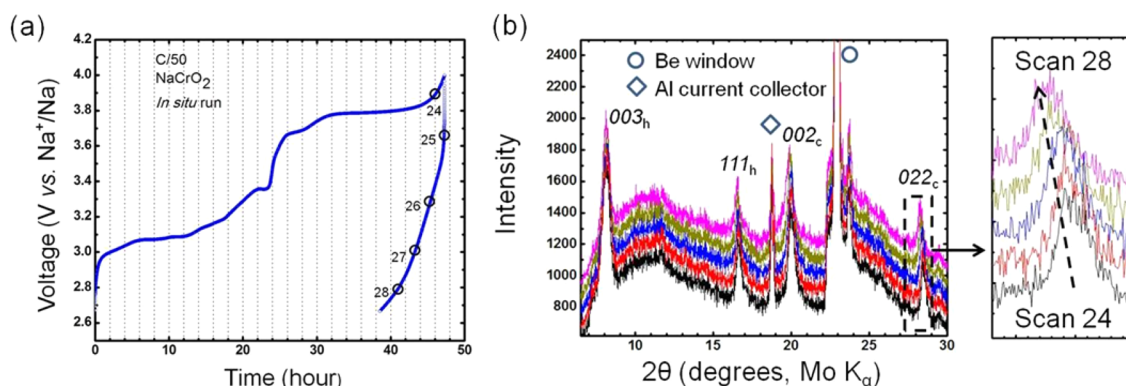
Figure 8. (a, b) Electrochemistry curve and *in situ* diffraction patterns (from scans 24 to 28) during discharge. The peaks corresponding to the O3 $Na_\delta CrO_2$ and rock-salt CrO_2 phases are marked with hkl_h and hkl_c, respectively.

$$\begin{pmatrix} -0.5 & 0 & 1 \\ 0.5 & -0.5 & 1 \\ 0 & 0.5 & 1 \end{pmatrix}$$

The transformed lattice parameters of the rock-salt phase in the hexagonal setting are $a = b = 2.8834$ Å, $c = 7.0630$ Å, which match almost perfectly with the lattice parameters of the O3 $Na_\delta CrO_2$ phase (note that the c lattice parameter of rock-salt CrO_2 is one-half of that in $R\bar{3}m$ because of the removal of cation ordering in a rock-salt lattice), which is consistent with the electron diffraction study discussed earlier. A notable difference between the O3 and rock-salt phases is that tetrahedrally coordinated Cr is present in the O3 phase but not in the rock-salt phase. The presence of tetrahedrally coordinated Cr was also observed in a previous XAS study performed by the Komaba group.[35] On the basis of the refinement results, the O3 phase can be written as $Cr_{0.67}^{oct}Cr_{0.33}^{tet}O_2$, where the superscripts are used to denote the coordination environment of Cr. Although the likely presence of Na^+ in the O3 $Na_\delta CrO_2$ phase will modify the refined Cr occupancy on different sites, the conclusions that Cr occupies both the octahedral and tetrahedral sites should be robust because the Rietveld refinements based on structural models where Cr occupies only octahedral or tetrahedral sites yield substantially worse fits (only octahedra, $R_{wp} = 9.015$; only tetrahedra, $R_{wp} = 8.879$; octahedra + tetrahedra, $R_{wp} = 8.624$). The refined structure of the O3 $Na_\delta CrO_2$ phase suggests that this O3 phase not only shares almost the same lattice dimensions as the rock-salt phase but also serves as an intermediate phase for the layered P′3 to rock-salt transformation in which the Cr cations are temporarily trapped in the tetrahedral sites. Once the structural parameters for the O3 $Na_\delta CrO_2$ and rock-salt CrO_2 phases are obtained, we can perform a Rietveld analysis on the diffraction data of the sample at the middle of the 3.8 V plateau based on a three-phase model (O3 CrO_2, rock-salt CrO_2, and P′3 $Na_{0.4}CrO_2$). As expected, a satisfactory fit was obtained. Taken together, these refinement results indicate that the P′3 $Na_{0.4}CrO_2$ phase is first converted into O3 $Na_\delta CrO_2$ in the P′3–X phase transition and that the latter phase will slowly transform into the rock-salt CrO_2 phase via redistribution of the Cr cations.

The layered-to-rock-salt transformation has two major detrimental effects on the intercalation process. First, the presence of Cr in the Na layer will block the Na diffusion channels and results in a reduced degree of Na intercalation that is likely accompanied by a large polarization. Second, as the

mobility of multivalent Cr^{n+} cations is much worse than that of monovalent Na^+, the reintercalation process will likely proceed via a kinetically favored pathway rather than following the thermodynamic equilibrium pathway (i.e., the rock-salt to layered transformation) because the time scale for Na intercalation should be much shorter than the substantial rearrangement of Cr cations. The reduced degree of Na intercalation, large kinetic barrier, and irreversibility are indeed observed during the discharge process of the $NaCrO_2$ following the 4 V charge (Figure 8). The Na intercalation appears to follow a solid-solution pathway rather than a multiphase reaction (i.e., rock-salt to O3 and P′3), as evidenced in the *in situ* XRD patterns (Figure 8), where a continuous shift of the diffraction peaks toward lower angles is observed.

The fact that even the large cation Na^+ (ionic radius of 1.02 Å) can intercalate into the mixture of rock-salt CrO_2 and O3 $Na_\delta CrO_2$ phases motivated us to investigate the possibility of Li intercalation into the same hosts, as the much smaller Li^+ (ionic radius of 0.76 Å) will have the opportunity to access the empty tetrahedral sites, which are inaccessible to the large Na^+ ions. As demonstrated in Figure 9, the Li^+ intercalation process is reversible, although this process is limited to only ∼0.15 Li insertion per formula unit and is associated with large polarizations (∼0.8 and ∼2.0 V for processes above and below 3 V, respectively). This result highlights the importance of Li excess in the intercalation chemistry of disordered rock-salt materials, as discussed in our recent publications.[50−52] The
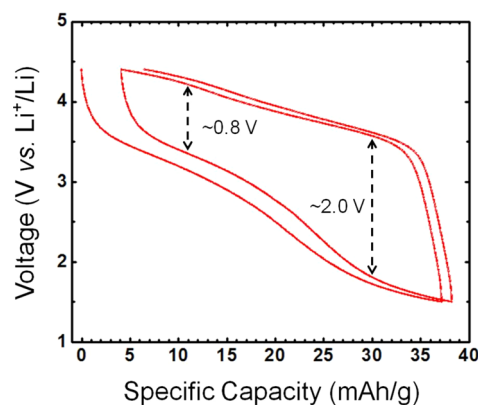

Figure 9. First and second cycles of fully charged $NaCrO_2$ vs Li metal in a 1 M $LiPF_6$ electrolyte. The battery was cycled between 1.5 and 4.4 V (vs Li^+/Li) under a rate of C/20.
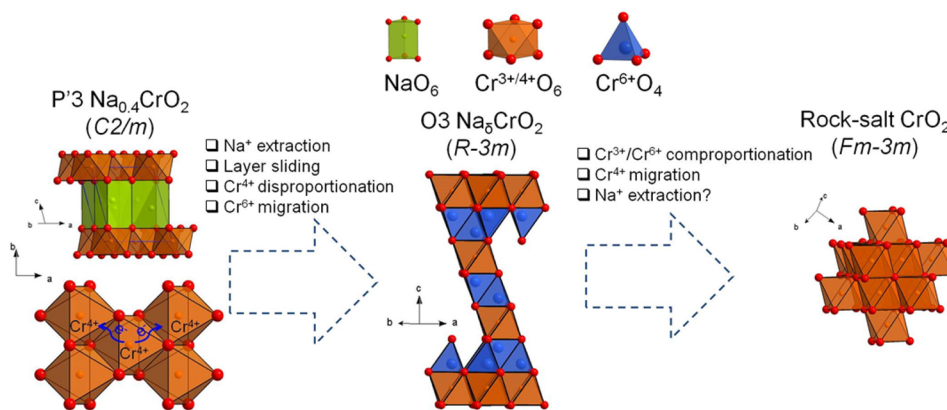
Figure 10. Proposed schematics of the layered P'3 $Na_{0.4}CrO_2$ to rock-salt CrO_2 structural transition.

Li excess introduces octahedral and tetrahedral vacant sites surrounded by Li cations only, making it easier for these sites to be accessed by Li ions than those sites surrounded by multivalent transition metal cations (e.g., Cr^{n+}).

DISCUSSION

Disproportionation-Assisted Layered-to-Rock-Salt Transformation. The mechanisms of transition metal migration induced structural transitions, such as layered-to-rock-salt and layered-to-spinel transformations, have been discussed in great detail in prior studies on related lithium layered oxides,[51,53−55] providing a strong foundation for the understanding of the current work. The mobility of a transition metal cation depends on its relative tetrahedral/octahedral site energy preference, which in turn is determined by its electronic structure.

In the cubic close-packed structures of $LiMO_2$ (M = Ti, V, Cr, Mn, Fe, Co, Ni), Cr and Mn cations are observed to exhibit relatively higher mobility when delithiated, making the layered-to-rock-salt or layered-to-spinel transformations more susceptible in Cr- and Mn-based $LiMO_2$ compounds. Cr-based compounds are often observed to transform into rock-salt phases,[51,56] whereas Mn-based compounds exhibit a strong tendency to form spinel-like structures,[54] hinting that the different electronic structures of Cr and Mn may play a critical role in determining the structural transformation pathways (i.e., layered to rock-salt vs layered to spinel).

There are two known factors that can facilitate the Cr migration in lithium layered oxides. One is the charge disproportionation of Cr^{4+} (3 Cr^{4+} → 2 Cr^{3+} + Cr^{6+}), which also applies to the Na analogues,[53] and the other is the formation of a dumbbell defect, which is energetically less favorable in the Na systems because of the much larger size of Na^+ compared with that of Li^+.[57] We argue that the Cr migration in lithium layered structures is initiated via the disproportionation of Cr^{4+} and the migration of the resulting Cr^{6+} into the tetrahedral site in the Li layer for two reasons. First, the small Cr^{6+} cation prefers the tetrahedral site, and second, although Cr^{3+} and Cr^{4+} prefer octahedral sites, thus hindering the migration to tetrahedral sites, Cr^{6+} with no 3d electrons has no preference. Indeed, reversible Cr^{6+} migration has been observed in $Li_{1.2}Cr_{0.4}Mn_{0.4}O_2$ through Cr L-edge X-ray absorption near-edge structure (XANES) measurements.[58] Noting that disproportionation is linked with the intrinsic chemical instability of the Cr^{4+} cations, the disproportionation-

assisted phase transition can, therefore, also apply to the Na analogues.[25,35]

The layered-to-rock-salt transformation process (or P'3 $Na_{0.4}CrO_2$ to rock-salt CrO_2) in desodiated $NaCrO_2$ can be rationalized based on the above considerations. As shown in the schematics of Figure 10, we propose that the first step in this structural transition involves layer sliding and Na^+ extraction that converts the P'3-type structure into an O3-type structure. Accompanying this process is the charge disproportion of Cr^{4+}, in which Cr^{6+} cations are generated and drop into the tetrahedral sites in the Na layer. The tetrahedrally coordinated Cr^{6+} cations will likely undergo a subsequent comproportionation reaction with two neighboring Cr^{3+} cations, reforming the Cr^{4+} cations that will escape the tetrahedral sites and eventually enter the permanent octahedral sites in the Na layer. Because the complex charge transfer and migration of highly charged Cr cations are expected to be slow, a kinetically trapped intermediate phase, i.e., O3 $Na_{\delta}CrO_2$, may be created in which part of the Cr cations have migrated to the temporary tetrahedral sites in the Na layer, resulting in a composition of $Cr_{0.67}^{oct}Cr_{0.33}^{tet}O_2$. We note that our current data set cannot unambiguously determine if this intermediate state with tetrahedral Cr is a true phase or just part of the continuous transition from O3 $Na_{\delta}CrO_2$ to rock-salt CrO_2.

Suppressing the Layered-to-Rock-Salt Transformation via Chemical Substitutions. When limiting the charge process to 0.5 Na extraction, $NaCrO_2$ has been demonstrated to possess excellent cyclability, rate capability, and thermal stability.[17,33] For practical applications, however, the energy density (i.e., specific capacity and/or operation voltage) of $NaCrO_2$ still must be improved. On the basis of the current work, the key to fully unlocking the potential of $NaCrO_2$ cathodes is to suppress the layered-to-rock-salt transformation such that a higher reversible capacity can be achieved.

Two steps are required for this layered-to-rock-salt structural transformation to occur: (1) conversion of the P'3 structure of $Na_{0.4}CrO_2$ into an O3-type structure that involves layer sliding and Na^+ extraction and (2) Cr^{4+} disproportionation, producing Cr^{6+}, which can move into the tetrahedral sites in the Na layer of the O3 intermediate structure. The P'3-to-O3 structural transition is driven by thermodynamics. Figure 11 shows the energy difference between the P3 and O3 stacking as a function of Na content. O3 is the stacking that occurs with lower energy at high and low Na content, and P3 is the stacking that occurs with lower energy at intermediate Na content. It should be noted that we did not consider van der Waals interactions in
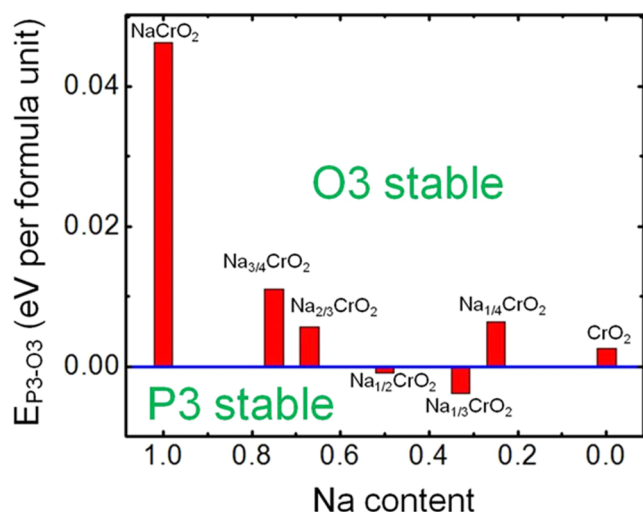
Figure 11. Energy difference between P3 and O3 as a function of Na content (Na$_x$CrO$_2$) evaluated through *ab initio* DFT calculations at 0 K.

these calculations, which may slightly modify the energy difference between the O3 and P3 phases, particularly at low Na content.[59] The disproportionation of Cr^{4+} most likely requires three Cr^{4+} cations to be in close proximity such that charge transfer among them can occur. Therefore, it appears that the most effective strategy to suppress the layered-to-rock-salt transformation is to reduce the concentration of Cr^{4+} triplets through chemical substitutions such that the degree of Cr^{4+} disproportionation is reduced.

The disproportionation-assisted phase transition in NaCrO$_2$ is very similar to the layered-to-spinel transformation in LiMnO$_2$, where Mn^{3+} cations disproportionate into mobile Mn^{2+} and immobile Mn^{4+}.[54] This suggests that a similar substitution strategy might be utilized to suppress the layered-to-rock-salt transformation in NaCrO$_2$. However, we highlight some important distinctions between NaCrO$_2$ and LiMnO$_2$ that need to be considered in the materials design process. Mn^{3+} disproportionation occurs via two Mn^{3+} cations exchanging electrons. To reduce the probability of finding Mn^{3+}–Mn^{3+} pairs, e.g., by 50%, a substitution level of ~30% (e.g., LiMn$_{0.7}$X$_{0.3}$O$_2$, where X denotes a trivalent cation) is needed (0.7 × 0.7 = 0.49, assuming a complete random distribution of cations without short-range ordering). The required substitution level is significantly reduced in NaCrO$_2$ because the Cr^{4+} disproportionation depends on the presence of Cr^{4+}–Cr^{4+}–Cr^{4+} triplets. To reach the same 50% probability reduction, only ~20% substitution is needed in the Cr system (0.8 × 0.8 × 0.8 = 0.51). It is intriguing to note that Cr disproportionation and migration appear to be completely suppressed in P2 Na$_{0.6}$(Cr$_{0.6}$Ti$_{0.4}$)O$_2$,[60] which may be an outcome of the reduced concentration of Cr^{4+} triplets, as discussed above. The chemical substitution can be performed via the introduction of isovalent (or 3+) cations or aliovalent cations. When using a redox-active isovalent substituent, the oxidized form of the substituent cation (e.g., Ti^{4+}) must be less electronegative than that of Cr^{4+} such that it does not accept electrons from Cr^{4+} to trigger the disproportionation reaction. Another factor to consider is whether the mixed compound can be synthesized. As the synthesis of NaCrO$_2$ is often performed under an inert atmosphere, the mixing of Cr^{3+} with any other cation that requires an oxidizing atmosphere in the synthesis

will be unlikely, e.g., Ni^{3+}. Instead of isovalent substitution, a more complicated substitution strategy could also be explored, such as the replacement of Cr^{3+} with two types of cations, where one cation is lower than 3+ and the other is higher than 3+ (e.g., Fe^{2+}/Ti^{4+} and Li$^+$/Nb^{5+}).

■ CONCLUSIONS

In this work, we demonstrated through a combined *in situ/ex situ* XRD, electron microscopy, electrochemistry, and *ab initio* study that the layered P′3 Na$_{0.4}$CrO$_2$ to rock-salt CrO$_2$ phase transition is responsible for the capacity decay observed in NaCrO$_2$. This layered-to-rock-salt transformation is completed via Cr^{4+} disproportionation/comproportionation and the formation of a metastable intermediate O3 CrO$_2$ phase. In addition, we observed no sign of Cr migration in the P′3 Na$_{0.4}$CrO$_2$ phase through Rietveld analysis of synchrotron XRD data, which explains the reversibility of NaCrO$_2$ when limiting the charge process to no more than 0.5 Na extraction. The fundamental insights into the layered-to-rock-salt transformation process in NaCrO$_2$ obtained from this work provide a strong basis for future materials design of NaCrO$_2$ and other related layered oxides as electrodes for battery applications. This work also highlights the general tendency for the structure of Cr-based O3 compounds (either Na or Li oxides) to transform into a rock-salt-like structure during deintercalation of the alkaline ions, motivating a further theoretical and/or experimental investigation toward the understanding of the intrinsic physical and chemical origins of this process.

■ ASSOCIATED CONTENT

ⓢ Supporting Information
The Supporting Information is available free of charge on the ACS Publications website at DOI: 10.1021/acs.chemmater.5b04626.

> Diffraction patterns of the pristine and partially desodiated NaCrO$_2$ and the associated structural parameters (PDF)

■ AUTHOR INFORMATION

Corresponding Author
*E-mail: gceder@mit.edu.
Author Contributions
⊥S.-H.B. and X.L. contributed equally to this work.
Notes
The authors declare no competing financial interest.

■ ACKNOWLEDGMENTS

■ REFERENCES

(1) Palomares, V.; Casas-Cabanas, M.; Castillo-Martinez, E.; Han, M. H.; Rojo, T. Update on Na-based battery materials. A growing research path. *Energy Environ. Sci.* **2013**, *6*, 2312–2337.
(2) Kim, S.-W.; Seo, D.-H.; Ma, X.; Ceder, G.; Kang, K. Electrode Materials for Rechargeable Sodium-Ion Batteries: Potential Alter-

natives to Current Lithium-Ion Batteries. *Adv. Energy Mater.* **2012**, *2*, 710−721.

(3) Ellis, B. L.; Nazar, L. F. Sodium and sodium-ion energy storage batteries. *Curr. Opin. Solid State Mater. Sci.* **2012**, *16*, 168−177.

(4) Slater, M. D.; Kim, D.; Lee, E.; Johnson, C. S. Sodium-Ion Batteries. *Adv. Funct. Mater.* **2013**, *23*, 947−958.

(5) Yabuuchi, N.; Kubota, K.; Dahbi, M.; Komaba, S. Research Development on Sodium-Ion Batteries. *Chem. Rev.* **2014**, *114*, 11636− 11682.

(6) Billaud, J.; Clément, R. J.; Armstrong, A. R.; Canales-Vázquez, J.; Rozier, P.; Grey, C. P.; Bruce, P. G. β-NaMnO2: A High-Performance Cathode for Sodium-Ion Batteries. *J. Am. Chem. Soc.* **2014**, *136*, 17243−17248.

(7) Xu, J.; Lee, D. H.; Clément, R. J.; Yu, X.; Leskes, M.; Pell, A. J.; Pintacuda, G.; Yang, X.-Q.; Grey, C. P.; Meng, Y. S. Identifying the Critical Role of Li Substitution in P2−Na$_x$[Li$_y$Ni$_z$Mn$_{1−y−z}$]O$_2$ (0 < x, y, z < 1) Intercalation Cathode Materials for High-Energy Na-Ion Batteries. *Chem. Mater.* **2014**, *26*, 1260−1269.

(8) Ellis, B. L.; Makahnouk, W. R. M.; Makimura, Y.; Toghill, K.; Nazar, L. F. A multifunctional 3.5 V iron-based phosphate cathode for rechargeable batteries. *Nat. Mater.* **2007**, *6*, 749−753.

(9) Ma, J.; Bo, S.-H.; Wu, L.; Zhu, Y.; Grey, C. P.; Khalifah, P. G. Ordered and Disordered Polymorphs of Na(Ni$_{2/3}$Sb$_{1/3}$)O$_2$: Honeycomb-Ordered Cathodes for Na-Ion Batteries. *Chem. Mater.* **2015**, *27*, 2387−2399.

(10) Li, X.; Wu, D.; Zhou, Y.-N.; Liu, L.; Yang, X.-Q.; Ceder, G. O3-type Na(Mn$_{0.25}$Fe$_{0.25}$Co$_{0.25}$Ni$_{0.25}$)O$_2$: A quaternary layered cathode compound for rechargeable Na ion batteries. *Electrochem. Commun.* **2014**, *49*, 51−54.

(11) Liu, J.; Chang, D.; Whitfield, P.; Janssen, Y.; Yu, X.; Zhou, Y.; Bai, J.; Ko, J.; Nam, K.-W.; Wu, L.; Zhu, Y.; Feygenson, M.; Amatucci, G.; Van der Ven, A.; Yang, X.-Q.; Khalifah, P. Ionic Conduction in Cubic Na$_3$TiP$_3$O$_9$N, a Secondary Na-Ion Battery Cathode with Extremely Low Volume Change. *Chem. Mater.* **2014**, *26*, 3295−3305.

(12) Yabuuchi, N.; Kajiyama, M.; Iwatate, J.; Nishikawa, H.; Hitomi, S.; Okuyama, R.; Usui, R.; Yamada, Y.; Komaba, S. P2-type Na$_x$[Fe$_{1/2}$Mn$_{1/2}$]O$_2$ made from earth-abundant elements for rechargeable Na batteries. *Nat. Mater.* **2012**, *11*, 512−517.

(13) Kim, D.; Lee, E.; Slater, M.; Lu, W.; Rood, S.; Johnson, C. S. Layered Na[Ni$_{1/3}$Fe$_{1/3}$Mn$_{1/3}$]O$_2$ cathodes for Na-ion battery application. *Electrochem. Commun.* **2012**, *18*, 66−69.

(14) Vassilaras, P.; Ma, X.; Li, X.; Ceder, G. Electrochemical Properties of Monoclinic NaNiO$_2$. *J. Electrochem. Soc.* **2013**, *160*, A207−A211.

(15) Kikkawa, S.; Miyazaki, S.; Koizumi, M. Deintercalated NaCoO$_2$ and LiCoO$_2$. *J. Solid State Chem.* **1986**, *62*, 35−39.

(16) Ma, X.; Chen, H.; Ceder, G. Electrochemical Properties of Monoclinic NaMnO$_2$. *J. Electrochem. Soc.* **2011**, *158*, A1307−A1312.

(17) Komaba, S.; Takei, C.; Nakayama, T.; Ogata, A.; Yabuuchi, N. Electrochemical intercalation activity of layered NaCrO$_2$ vs. LiCrO$_2$. *Electrochem. Commun.* **2010**, *12*, 355−358.

(18) Didier, C.; Guignard, M.; Denage, C.; Szajwaj, O.; Ito, S.; Saadoune, I.; Darriet, J.; Delmas, C. Electrochemical Na-Deintercalation from NaVO$_2$. *Electrochem. Solid-State Lett.* **2011**, *14*, A75−A78.

(19) Wu, D.; Li, X.; Xu, B.; Twu, N.; Liu, L.; Ceder, G. NaTiO$_2$: a layered anode material for sodium-ion batteries. *Energy Environ. Sci.* **2015**, *8*, 195−202.

(20) Maazaz, A.; Delmas, C.; Hagenmuller, P. A study of the Na$_x$TiO$_2$ system by electrochemical deintercalation. *J. Inclusion Phenom.* **1983**, *1*, 45−51.

(21) Takeda, Y.; Nakahara, K.; Nishijima, M.; Imanishi, N.; Yamamoto, O.; Takano, M.; Kanno, R. Sodium deintercalation from sodium iron oxide. *Mater. Res. Bull.* **1994**, *29*, 659−666.

(22) Delmas, C.; Fouassier, C.; Hagenmuller, P. Structural classification and properties of the layered oxides. *Physica B+C* **1980**, *99*, 81−85.

(23) Yoshida, H.; Yabuuchi, N.; Komaba, S. NaFe$_{0.5}$Co$_{0.5}$O$_2$ as high energy and power positive electrode for Na-ion battery. *Electrochem. Commun.* **2013**, *34*, 60−63.

(24) Yabuuchi, N.; Yoshida, H.; Komaba, S. Crystal structures and electrode performance of alpha-NaFeO$_2$ for rechargeable sodium batteries. *Electrochemistry* **2012**, *80*, 716−719.

(25) Komaba, S.; Nakayama, T.; Ogata, A.; Shimizu, T.; Takei, C.; Takada, S.; Hokura, A.; Nakai, I. Electrochemically Reversible Sodium Intercalation of Layered NaNi$_{0.5}$Mn$_{0.5}$O$_2$ and NaCrO$_2$. *Ecs Transactions* **2008**, *16*, 43−55.

(26) Buchholz, D.; Chagas, L. G.; Vaalma, C.; Wu, L.; Passerini, S. Water sensitivity of layered P2/P3-Na$_x$Ni$_{0.22}$Co$_{0.11}$Mn$_{0.66}$O$_2$ cathode material. *J. Mater. Chem. A* **2014**, *2*, 13415−13421.

(27) Duffort, V.; Talaie, E.; Black, R.; Nazar, L. F. Uptake of CO$_2$ in Layered P2-Na$_{0.67}$Mn$_{0.5}$Fe$_{0.5}$O$_2$: Insertion of Carbonate Anions. *Chem. Mater.* **2015**, *27*, 2515−2524.

(28) Lu, Z.; Dahn, J. R. Intercalation of Water in P2, T2 and O2 Structure A$_z$[Co$_x$Ni$_{1/3−x}$Mn$_{2/3}$]O$_2$. *Chem. Mater.* **2001**, *13*, 1252−1257.

(29) Van der Ven, A.; Aydinol, M. K.; Ceder, G.; Kresse, G.; Hafner, J. First-principles investigation of phase stability in Li$_x$CoO$_2$. *Phys. Rev. B: Condens. Matter Mater. Phys.* **1998**, *58*, 2975−2987.

(30) Braconnier, J. J.; Delmas, C.; Hagenmuller, P. Etude par desintercalation electrochimique des systemes Na$_x$CrO$_2$ et Na$_x$NiO$_2$. *Mater. Res. Bull.* **1982**, *17*, 993−1000.

(31) Miyazaki, S.; Kikkawa, S.; Koizumi, M. Chemical and electrochemical deintercalations of the layered compounds LiMO$_2$ (M = Cr, Co) and NaM′O$_2$ (M′ Cr, Fe, Co, Ni). *Synth. Met.* **1983**, *6*, 211−217.

(32) Xia, X.; Dahn, J. R. NaCrO$_2$ is a Fundamentally Safe Positive Electrode Material for Sodium-Ion Batteries with Liquid Electrolytes. *Electrochem. Solid-State Lett.* **2012**, *15*, A1−A4.

(33) Yu, C.-Y.; Park, J.-S.; Jung, H.-G.; Chung, K.-Y.; Aurbach, D.; Sun, Y.-K.; Myung, S.-T. NaCrO$_2$ cathode for high-rate sodium-ion batteries. *Energy Environ. Sci.* **2015**, *8*, 2019−2026.

(34) Zhou, Y.-N.; Ding, J.-J.; Nam, K.-W.; Yu, X.; Bak, S.-M.; Hu, E.; Liu, J.; Bai, J.; Li, H.; Fu, Z.-W.; Yang, X.-Q. Phase transition behavior of NaCrO$_2$ during sodium extraction studied by synchrotron-based X-ray diffraction and absorption spectroscopy. *J. Mater. Chem. A* **2013**, *1*, 11130−11134.

(35) Kubota, K.; Ikeuchi, I.; Nakayama, T.; Takei, C.; Yabuuchi, N.; Shiiba, H.; Nakayama, M.; Komaba, S. New Insight into Structural Evolution in Layered NaCrO$_2$ during Electrochemical Sodium Extraction. *J. Phys. Chem. C* **2015**, *119*, 166−175.

(36) Arroyo y de Dompablo, M. E.; Ceder, G. First-principles calculations on Li$_x$NiO$_2$: phase stability and monoclinic distortion. *J. Power Sources* **2003**, *119-121*, 654−657.

(37) Jain, A.; Hautier, G.; Moore, C. J.; Ong, S. P.; Fischer, C. C.; Mueller, T.; Persson, K. A.; Ceder, G. A high-throughput infrastructure for density functional theory calculations. *Comput. Mater. Sci.* **2011**, *50*, 2295−2310.

(38) Kresse, G.; Furthmüller, J. Efficient iterative schemes for ab initio total-energy calculations using a plane-wave basis set. *Phys. Rev. B: Condens. Matter Mater. Phys.* **1996**, *54*, 11169.

(39) Blöchl, P. E. Projector augmented-wave method. *Phys. Rev. B: Condens. Matter Mater. Phys.* **1994**, *50*, 17953.

(40) Perdew, J. P.; Ernzerhof, M.; Burke, K. Rationale for mixing exact exchange with density functional approximations. *J. Chem. Phys.* **1996**, *105*, 9982−9985.

(41) Anisimov, V. I.; Aryasetiawan, F.; Lichtenstein, A. I. First-principles calculations of the electronic structure and spectra of strongly correlated systems: the LDA+ U method. *J. Phys.: Condens. Matter* **1997**, *9*, 767.

(42) Wang, L.; Maxisch, T.; Ceder, G. Oxidation energies of transition metal oxides within the GGA+ U framework. *Phys. Rev. B: Condens. Matter Mater. Phys.* **2006**, *73*, 195107.

(43) Sathiya, M.; Hemalatha, K.; Ramesha, K.; Tarascon, J. M.; Prakash, A. S. Synthesis, structure, and electrochemical properties of the layered sodium insertion cathode material: NaNi$_{1/3}$Mn$_{1/3}$Co$_{1/3}$O$_2$. *Chem. Mater.* **2012**, *24*, 1846−1853.

(44) Lei, Y.; Li, X.; Liu, L.; Ceder, G. Synthesis and stoichiometry of different layered sodium cobalt oxides. *Chem. Mater.* **2014**, *26*, 5288− 5296.

(45) Han, M. H.; Gonzalo, E.; Casas-Cabanas, M.; Rojo, T. Structural evolution and electrochemistry of monoclinic $NaNiO_2$ upon the first cycling process. *J. Power Sources* **2014**, *258*, 266−271.

(46) Li, X.; Ma, X.; Su, D.; Liu, L.; Chisnell, R.; Ong, S. P.; Chen, H.; Toumar, A.; Idrobo, J.-C.; Lei, Y.; et al. Direct visualization of the Jahn−Teller effect coupled to Na ordering in $Na_{5/8}MnO_2$. *Nat. Mater.* **2014**, *13*, 586−592.

(47) Stephens, P. W. Phenomenological model of anisotropic peak broadening in powder diffraction. *J. Appl. Crystallogr.* **1999**, *32*, 281−289.

(48) Adams, S. Relationship between bond valence and bond softness of alkali halides and chalcogenides. *Acta Crystallogr., Sect. B: Struct. Sci.* **2001**, *57*, 278−287.

(49) Aroyo, M. I.; Perez-Mato, J. M.; Capillas, C.; Kroumova, E.; Ivantchev, S.; Madariaga, G.; Kirov, A.; Wondratschek, H. Bilbao Crystallographic Server: I. Databases and crystallographic computing programs. *Z. Kristallogr. - Cryst. Mater.* **2006**, *221*, 15−27.

(50) Urban, A.; Lee, J.; Ceder, G. The Configurational Space of Rocksalt-Type Oxides for High-Capacity Lithium Battery Electrodes. *Adv. Energy Mater.* **2014**, *4*, DOI: 10.1002/aenm.201400478.

(51) Lee, J.; Urban, A.; Li, X.; Su, D.; Hautier, G.; Ceder, G. Unlocking the potential of cation-disordered oxides for rechargeable lithium batteries. *Science* **2014**, *343*, 519−522.

(52) Twu, N.; Li, X.; Urban, A.; Balasubramanian, M.; Lee, J.; Liu, L.; Ceder, G. Designing New Lithium-Excess Cathode Materials from Percolation Theory: Nanohighways in $Li_xNi_{2−4x/3}Sb_{x/3}O2$. *Nano Lett.* **2015**, *15*, 596−602.

(53) Reed, J.; Ceder, G. Role of electronic structure in the susceptibility of metastable transition-metal oxide structures to transformation. *Chem. Rev.* **2004**, *104*, 4513−4534.

(54) Reed, J.; Ceder, G.; Van Der Ven, A. Layered-to-Spinel Phase Transition in Li_xMnO_2. *Electrochem. Solid-State Lett.* **2001**, *4*, A78−A81.

(55) Mohanty, D.; Li, J.; Abraham, D. P.; Huq, A.; Payzant, E. A.; Wood, D. L.; Daniel, C. Unraveling the Voltage-Fade Mechanism in High-Energy-Density Lithium-Ion Batteries: Origin of the Tetrahedral Cations for Spinel Conversion. *Chem. Mater.* **2014**, *26*, 6272−6280.

(56) Lyu, Y.; Ben, L.; Sun, Y.; Tang, D.; Xu, K.; Gu, L.; Xiao, R.; Li, H.; Chen, L.; Huang, X. Atomic insight into electrochemical inactivity of lithium chromate ($LiCrO_2$): Irreversible migration of chromium into lithium layers in surface regions. *J. Power Sources* **2015**, *273*, 1218−1225.

(57) Kim, S.; Ma, X.; Ong, S. P.; Ceder, G. A comparison of destabilization mechanisms of the layered Na_xMO_2 and Li_xMO_2 compounds upon alkali de-intercalation. *Phys. Chem. Chem. Phys.* **2012**, *14*, 15571−15578.

(58) Ammundsen, B.; Paulsen, J.; Davidson, I.; Liu, R.-S.; Shen, C.-H.; Chen, J.-M.; Jang, L.-Y.; Lee, J.-F. Local Structure and First Cycle Redox Mechanism of Layered $Li_{1.2}Cr_{0.4}Mn_{0.4}O_2$ Cathode Material. *J. Electrochem. Soc.* **2002**, *149*, A431−A436.

(59) Aykol, M.; Kim, S.; Wolverton, C. van der Waals Interactions in Layered Lithium Cobalt Oxides. *J. Phys. Chem. C* **2015**, *119*, 19053−19058.

(60) Wang, Y.; Xiao, R.; Hu, Y.-S.; Avdeev, M.; Chen, L. P2-$Na_{0.6}[Cr_{0.6}Ti_{0.4}]O_2$ cation-disordered electrode for high-rate symmetric rechargeable sodium-ion batteries. *Nat. Commun.* **2015**, *6*, 6954.